Supporting Information

Bias Switchable Narrowband/Broadband NIR Organic-Photodetector Fabricated with a Scalable Technique

Lai-Hung Lai[*a], Wei-Hsiang Lin[a], Chin-Chuan Hsieh[a], Maria Antonietta Loi[‡b]

[a.]   *Wafer Level Optics Organization, VisEra Technologies Company Limited, No. 12, Dusing Rd. 1Hsinchu Science Park, Hsinchu City 30078, Taiwan*

[b.]   *Photophysics and OptoElectronics, Zernike Institute for Advanced Materials, University of Groningen, Nijenborgh 4, 9747 AG Groningen, The Netherlands*

[*]E-mail: Larry_Lai@viseratech.com; [‡]m.a.loi@rug.nl Electronic

1. UV–vis spectra and energy-level diagram of the photoactive material
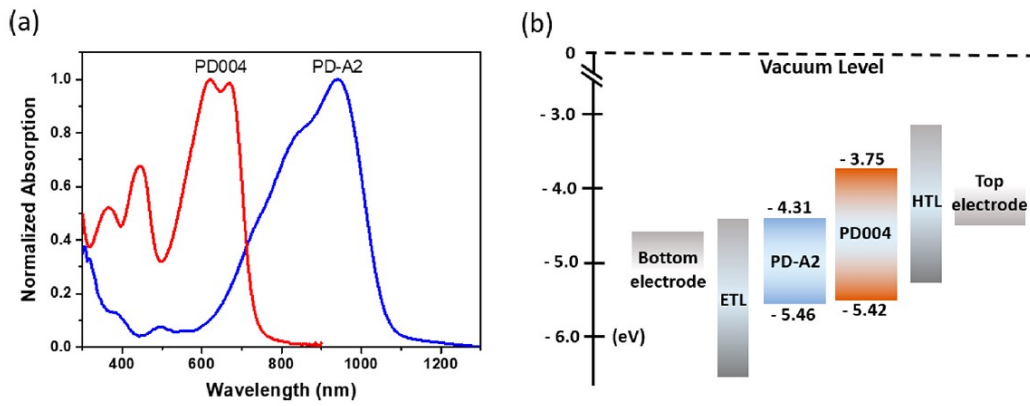
(a)

(b)

Figure S1. (a) UV–vis spectra and (b) energy diagram of the PD004:PD-A2 BHJ system.

2. Dark I-V curve fitting
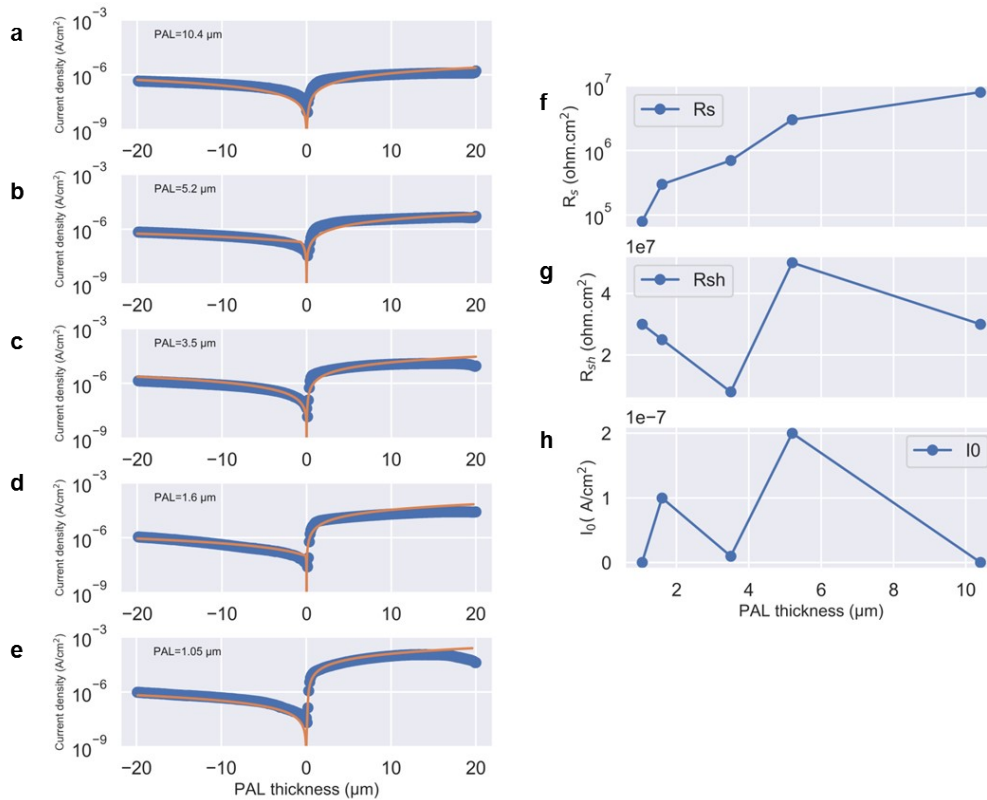
Figure S2. Dark IV curved and fitting summary.

Table S1. Summary of the fitting results.

PAL thickness (µm)	1.05	1.6	3.5	5.2	10.4
R_s (ohm.cm^2)	8.0E+04	3.0E+05	7.0E+05	3.0E+06	8.0E+06
R_{sh} (ohm.cm^2)	3.0E+07	2.5E+07	8.0E+06	5.0E+07	3.0E+07
I_0 (A/cm^2)	4.0E-10	1.0E-07	1.0E-08	2.0E-07	5.0E-10
n	1.1	1.1	1.1	1.1	1.1

3. Comparison between the state-of-the art Si CMOS image sensors with OPD.
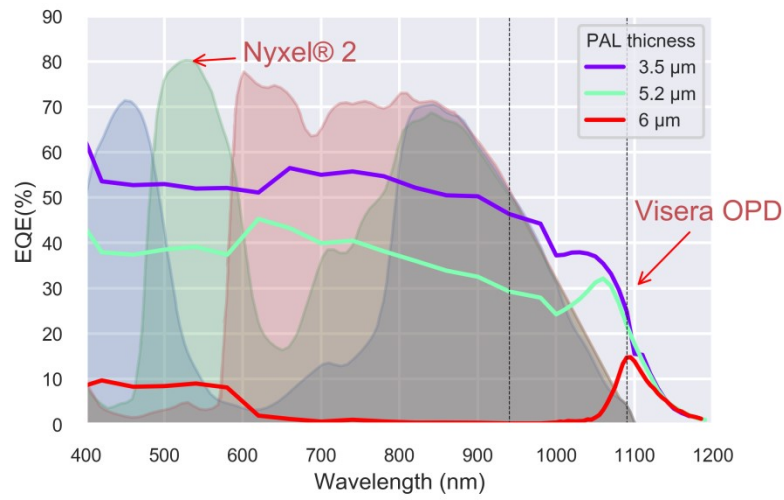
Figure S3. EQE spectra for the state-of-art commercial NIR Si image sensor (Nyxel® 2) and Visera's OPD photodetector made by blade coating with various active layers measured at -4V.

4. Absorption spectra of donor and acceptor thin film and the extinction coefficient of the photoactive layer
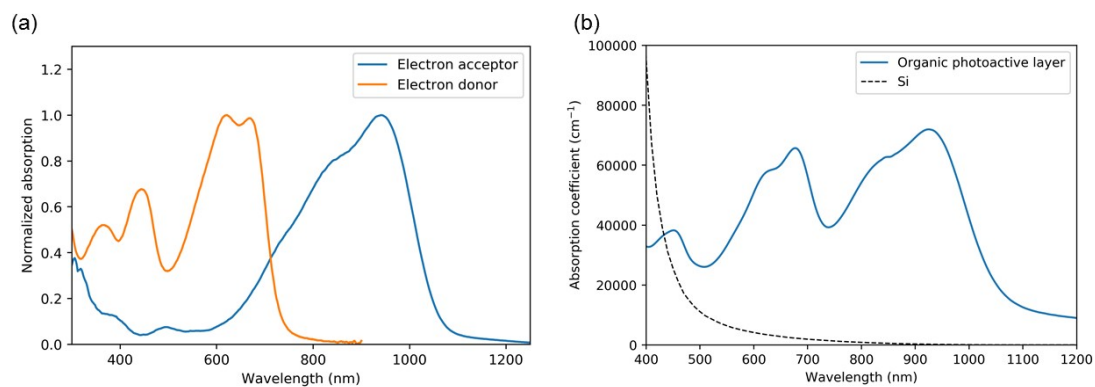
Figure S4. (a) The normalized absorption spectra of acceptor and donor thin film. (b) the absorption coefficient of the photoactive layer composed by a mixture of donor and acceptor. The black dash line shows the absorption coefficient of Si as a comparison.
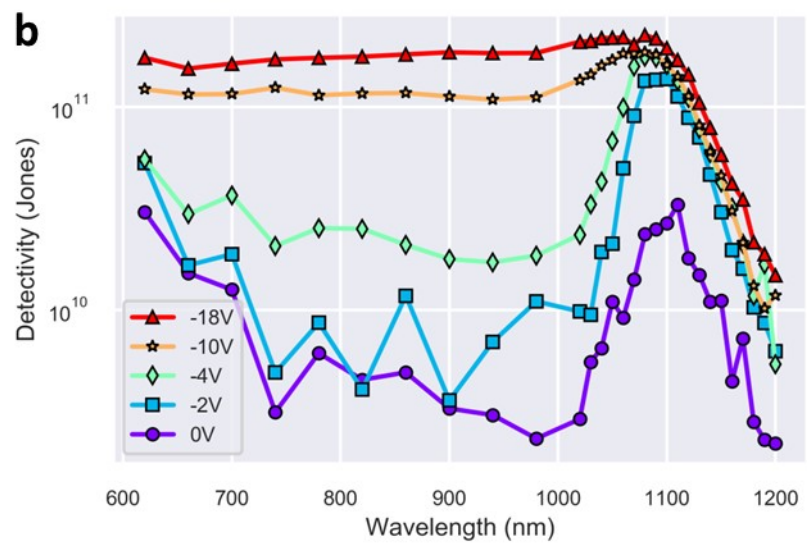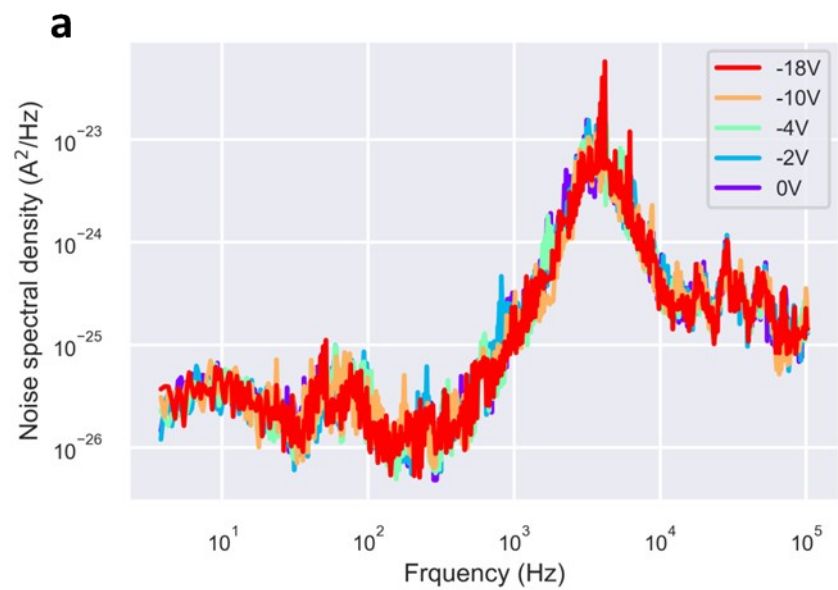
5. Summary of the photodetector performance

Table S2. Summary of the photodetector performance

	Unit	Bias	PAL Thickness (µm)						
			0.32	1.05	1.6	3.5	5.2	6	10.4
f_{-3db} at 4V	Hz		NA	23357	16238	5456	379	518	50
Dark current	A/cm^2	-2V	8.9e-6	5.5e-8	5.8e-8	1.1e-7	1.4e-7	8.0e-8	1.4e-7
		-4V	1.4e-5	8.2e-8	8.5e-8	1.7e-7	2.1e-7	1.2e-7	2.3e-7
		-10V	9.8e-6	2.7e-7	1.7e-7	3.3e-7	4.0e-7	2.5e-7	4.9e-7
EQE @940 nm	%	-2V	45.9	40.1	35.2	42.5	14.8	1.4	0.31
		-4V	47.0	46.3	46.2	46.4	29.3	3.7	0.2
		-10V	48.1	41.0	37.3	47.8	39.7	28.6	0.9
		-18V	NA	NA	NA	48.6	42.0	43.3	17.7
EQE @1100 nm	%	-2V	5.9	16.1	14.9	13.1	13.4	23.6	9.75
		-4V	6.2	17.2	23.1	15.5	17.7	29.5	13.9
		-10V	6.53	18.2	17.7	18.3	24.2	36.2	20.5
		-18V	NA	NA	NA	19.6	27.9	39.2	22.5

6. Noise spectral density and detectivity of organic photodetector

When considering the flicker noise (1/f-noise) and the thermal noise on the total noise current of the photodetectors, the detectivity is expressed as $D = R \times \sqrt{A}/S_n$, where R is responsivity, A is the device area, and S_n is the noise spectral density.

a

Noise spectral density (A²/Hz) vs Frequency (Hz)

Legend:
- -18V
- -10V
- -4V
- -2V
- 0V

b

Detectivity (Jones) vs Wavelength (nm)

Legend:
- -18V
- -10V
- -4V
- -2V
- 0V

Figure S5. (a) Noise spectral density of organic photodetector with 6 μm active layer thickness. (b) Detectivity of the photodetector by considering shot noise, flicker noise (1/f-noise) and thermal noise.

7. Summary of narrowband OPD performance from literatures.

Table S3. Summary of narrowband OPD performance from literatures.

Photo-absorbing materials	PAL thickness (nm)	Peak (nm)	FWHM (nm)	D* (Jones)	EQE (%]	R (A W-1)	Bias (V)	LDR (dB)	f −3dB (Hz)	Year	PAL deposition method	Ref.
3:PC61BM	150	500	130		8.2	0.03	−1.0			2013	Spin coating	1
2:PC61BM		525	80	1.00E+11	15	0.06	−1.0	80	25,000	2014	Spin coating	2
Cy7-T:C60		850	100	1.00E+12	17	0.12	−1.0			2015	Spin coating	3
DPP-DTT:PC70BM	2000	950	90	4.8E+12		0.06	-1	160	100,000	2015	Spin coating	4
PDTP-DFBT: PC71BM: PbS	4000	890	50	7.98E11	183	1.31	-7	110	360	2016	Drop casting	5
P3HT:PTB7-Th: PC61BM		800	40	3.00E+12			-10	180		2018	Drop casting	6
1(Pyrl):C60	15	481	76	2.00E+11	18	0.07	0			2019	Spin coating	7
PolyTPD:SBDTIC	70	740	141	1.42E+13	10.5	0.06	0	78	118,000	2019	Spin coating	8
PCZ-Th-DPP	300	709	170	4.60E+12			−1.0	109	1,200	2019	Spin coating	9
PCbisDPP:PC61BM		730	210	4.70E+11	80	0.31	−3.0			2019	Spin coating	10
PCE10:P3HT/PCBM	770	780		1E+12	4,5	0.027	-1	76.5	3500	2013	Spin coating	11
PCPDTBT:ZnO	70	725	175		68	0.4				2020	Spin coating	12
PSBOTz:PNDBO		530	155	1.00E+13	16.4	0.07	−2.0			2020	Spin coating	13
DT-PDPP2T-TT/Y6	800	940	66	1.6E+13		0.2				2020	Spin coating	14
1(Pyrl):1(Hex):C60		754	11	1.10E+10	14	0.086	0	61	150,000	2021	Spin coating	15
DMQA:SubPc		586	131	2.30E+12	60.1	0.27	−5.0			2013	Vacuum processing	16

| Material										Year	Processing	Ref
SubNc		690	180		80	0.45	−15.0			2015	Vacuum processing	[17]
DM-2,9-DMQA:SubPc		580	115	2.00E+12	56.5	0.26	−3.0		76700	2014	Vacuum processing	[18]
ISQ		680	80	3.20E+12	15		−2.0	114	190,000	2016	Vacuum processing	[19]
Rubrene:C60		470	80		55	0.21	−1.0		86,000	2016	Vacuum processing	[20]
M1:C60		550	67	3.73E+13	59	0.26	−3.0			2016	Vacuum processing	[21]
PSQ		600	110	7.70E+12	66	0.32	−2.5	96		2017	Vacuum processing	[22]
CiInPc:C60		705	190	3.30E+12	80	0.45	−1.0	77	2900	2019	Vacuum processing	[23]
1a:C60		560	97	4.37E+13	70	0.32	−3.0			2019	Vacuum processing	[24]
SubPc:C60		600	70	7.50E+11	16	0.08	−1.0			2021	Vacuum processing	[25]
PD940	6000	1100	61	1.17E+12	30	0.21	-2	>112	316 at -2V 1389 at -10V	2022	Blade coating	This work

8. Impedance fitting

The equivalent circuit shown in Figure S2(c1) is applied for EIS fitting, where R1 and CPE1 represent

bulk resistance and bulk chemical capacitance, respectively; R2 and CPE2 represent interface resistance

and interface chemical capacitance, respectively, and R3 represents series resistance.[26] The R_{bulk}

increases with increasing PAL thickness. The equivalent capacitance is calculated by $C = \dfrac{(R.CPE)^{1/n}}{R}$.

The RC time is $(R.CPE)^{1/n}$.
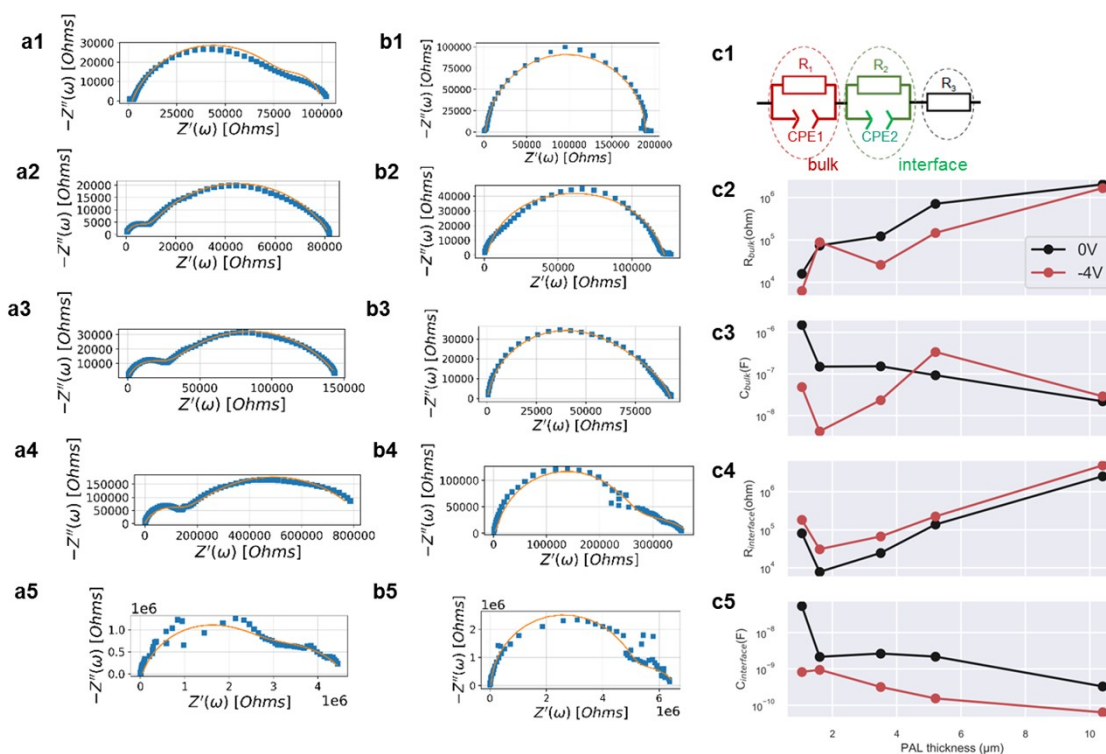
Figure S6. Impedance spectra measured at 0V (a1-a5) and -4V (b1-b5) under 520 nm LED illumination with intensity of 4.09 mW/cm² and their corresponding fitting results (orange line), (c1) equivalent circuit model for impedance fitting, where R1/CPE1 is related to the bulk, R2/CPE2 is related to the interface, and R3 us related to the series resistance. (c2-c5) the fitting results.

Table S4. Impedance fitting results at 0V

PAL thickness	R1	CPE1	n1		R2	CPE2	n2	R3
μm	ohm	F		s	ohm	F		ohm

1.05	1.60e+04	1.52e-06	1.00e+00	2.43e-02	8.16e+04	5.39e-08	7.69e-01	1.92e+03
1.6	7.42e+04	1.50e-07	6.45e-01	9.36e-04	7.87e+03	2.15e-09	8.23e-01	3.05e-29
3.5	1.22e+05	1.53e-07	6.16e-01	1.56e-03	2.46e+04	2.64e-09	7.84e-01	1.33e-19
5.2	7.15e+05	9.32e-08	5.85e-01	9.76e-03	1.37e+05	2.18e-09	7.43e-01	8.75e-29
10.4	2.05e+06	2.19e-08	5.98e-01	5.57e-03	2.53e+06	3.30e-10	8.08e-01	3.79e+04

Table S5. Impedance fitting results at -4V

PAL thickness	R1	CPE1	n1	τ1	R2	CPE2	n2	R3
µm	ohm	F		s	ohm	F		ohm
1.05	6.31e+03	4.85e-08	7.63e-01	2.48e-05	1.82e+05	8.25e-10	9.93e-01	1.57e+03
1.6	8.93e+04	4.14e-09	8.10e-01	5.79e-05	3.09e+04	9.47e-10	9.39e-01	1.85e+03
3.5	2.60e+04	2.34e-08	7.66e-01	6.34e-05	6.67e+04	3.19e-10	9.26e-01	1.19e+02
5.2	1.47e+05	3.39e-07	4.28e-01	9.05e-04	2.23e+05	1.54e-10	9.50e-01	2.43e+02
10.4	1.67e+06	2.90e-08	6.81e-01	1.17e-02	4.87e+06	6.38e-11	9.89e-01	3.88e+04

9. Optical simulation

The reflection and transmission of the structure are calculated using $R = \left|\dfrac{M_{21}}{M_{11}}\right|^2$ and

$T = \dfrac{n_s cos\theta_s}{n_0 cos\theta_0}\left|\dfrac{1}{M_{11}}\right|^2$, where M_{11} and M_{22} are derived from the matrix as follows.

$$\left[M_{11}\ M_{12}\ M_{21}\ M_{22}\right] = D_{12}P_2...D_{i-1,i}P_iD_{i,i+1}$$

,where $D_{i,i+1}$ is transmission matrix.

$$D_{i,i+1} = \dfrac{1}{t_{i,i+1}}\left[1\ r_{i,i+1}\ r_{i,i+1}\ M_{22}\right]$$

,where $r_{i,i+1}$ and $t_{i,i+1}$ are Fresnel reflection and transmission coefficients.

For TE light propagation,

$$r_{i,i+1} = \dfrac{\tilde{n}_i cos\theta_i - \tilde{n}_{i+1} cos\theta_{i+1}}{\tilde{n}_i cos\theta_i + \tilde{n}_{i+1} cos\theta_{i+1}}$$

$$t_{i,i+1} = \dfrac{2\tilde{n}_i cos\theta_i}{\tilde{n}_i cos\theta_i + \tilde{n}_{i+1} cos\theta_{i+1}}$$

For TM light propagation,

$$r_{i,i+1} = \frac{\tilde{n}_i cos\theta_{i+1} - \tilde{n}_{i+1} cos\theta_i}{\tilde{n}_i cos\theta_{i+1} + \tilde{n}_{i+1} cos\theta_i}$$

$$t_{i,i+1} = \frac{2\tilde{n}_i cos\theta_i}{\tilde{n}_i cos\theta_{i+1} + \tilde{n}_{i+1} cos\theta_i}$$

, where $\tilde{n}_i$ is the complex refractive index, $\tilde{n}_i = n_i + jk_i$.

The absorption in each layer is calculated from propagation matrix (P_i).

$$P_i = \left[e^{-j\phi_i} \; 0 \; 0 \; e^{j\phi_i} \right]$$

,where ϕ_i is the phase shift, $\phi_i = \frac{2\pi}{\lambda}\tilde{n}_i h_i$, where h_i is the thickness of i layer

Optical absorption (P_{abs}) is directly proportional to the whole E-field intensity ($|E|^2$). It can be expressed as

$$P_{abs} = \frac{1}{2}\omega\varepsilon_0 nk|E|^2$$

where ω is the angular frequency, ε_0 is the vacuum permittivity and n and k are the real and imaginary parts of the refractive index.[27,28,29]

10. Optical setup

The setup of NIR imaging by narrowband organic photodetector is shown in **Figure S5a**. The

monochromatic light at 1100 nm wavelength passing an optical chopper with a chopping frequency of

400 Hz is applied as a light source. The Si sample is placed on X-Z motorized stage and OPD is place on

next to the sample holder. The scanning of the image is done by moving the X-Z motorized stage

controlled by a microcontroller. The photocurrent at each scan point is acquired by a lock-in amplifier.

The setup for angularly and spectrally resolved EQE spectra is shown in **Figure S5b**. The monochromatic

light at various wavelengths passing an optical chopper with a chopping frequency of 400 Hz is applied

as a light source. The OPD is placed on a rotational stage. The photocurrent of OPD at each angle and

applied bias is acquired by a lock-in amplifier. The light intensity is calibrated by a Si (818-UV) and Ge

(818-IR) reference cell.
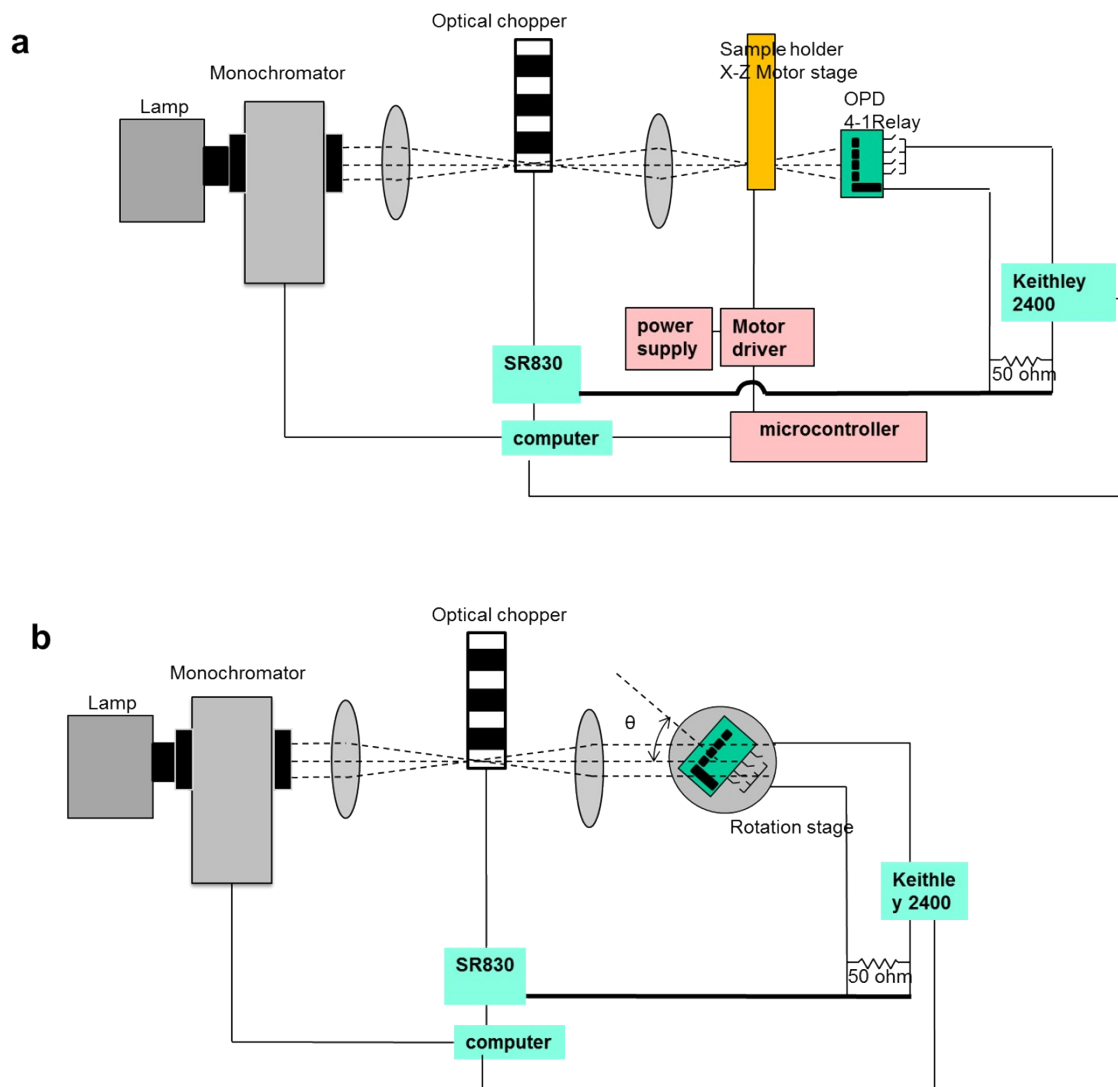
Figure S7. (a) Illustration of the image scanner setup composed of a light source, an x-z two-axis moving stage, and an organic photodetector readout circuit measured at the monochromatic light illumination of 1100 nm in transmission mode. (b) Illustration of the angular-dependent EQE scan setup.

References

[1] R. D. Jansen-Van Vuuren, A. Pivrikas, A. K. Pandey and P. L. Burn, *J. Mater. Chem. C,* 2013, *1*, 3532–3543.

[2] D. M. Lyons, A. Armin, M. Stolterfoht, R. C. R. Nagiri, R. D. Jansen-Van Vuuren, B. N. Pal, P. L. Burn, S. C. Lo and P. Meredith, *Org. Electron.,* 2014, *15*, 2903–2911.

[3] H. Zhang, S. Jenatsch, J. De Jonghe, F. Nuësch, R. Steim, A. C. Véron and R. Hany, *Sci. Rep.,* 2015, *5*, 9439.

[4] A. Armin, R. D. J.Vuuren, N. Kopidakis, P. L. Burn, P. Meredith, *Nat. Commun.,* 2015, *6*, 6343.

[5] L. Shen, Yang. Zhang, Y. Bai, X. Zheng, Q. Wang, J. Huang, Nanoscale, 2016, *8*, 12990.

[6] J. Miao, F. Zhang, M. Du, W. Wang, Y. Fang, *Adv. Opt. Mater.,* 2018, *6*, 1800001.

[7] A. Liess, A. Arjona-Esteban, A. Kudzus, J. Albert, A. M. Krause, A. Lv, M. Stolte, K. Meerholz and F. Würthner, *Adv. Funct. Mater.,* 2019, *29*, 1805058.

[8] K. Xia, Y. Li, Y. Wang, L. Portilla and V. Pecunia, *Adv. Opt. Mater.,* 2020, *8*, 1902056.

[9] S. Z. Hassan, H. J. Cheon, C. Choi, S. Yoon, M. Kang, J. Cho, Y. H. Jang, S. K. Kwon, D. S. Chung and Y. H. Kim, *ACS Appl. Mater. Interfaces,* 2019, *11*, 28106–28114.

[10] H. Opoku, B. Lim, E. S. Shin, H. Kong, J. M. Park, C. Bathula and Y. Y. Noh, Macromol. *Chem. Phys.,* 2019, *220*, 1900287.

[11] J. Kim, S. Yoon, K. M. Sim, D. S. Chung, *J. Mater. Chem. C*, **2019**, 7, 4770.

[12] J. Y. Kim, P. Vincent, J. Jang, M. S. Jang, M. Choi, J. H. Bae, C. Lee and H. Kim, *J. Alloys Compd.,* 2020, *813*, 152202.

[13] J. Kang, J. Kim, H. Ham, H. Ahn, S. Y. Lim, H. M. Kim, I. N. Kang and I. H. Jung, *Adv. Opt. Mater.,* 2020, *8*, 2001038.

[14] B. Xie, R. Xie, K. Zhang, Q. Yin, Z. Hu, G. Yu, F. Huang, Y. Cao, *Nat. Commun.,* 2020, *11*, 2871.

[15] T. Schembri, J. H. Kim, A. Liess, V. Stepanenko, M. Stolte and F. Würthner, *Adv. Opt. Mater.,* 2021, *9*, 2100213.

[16] K. H. Lee, D. S. Leem, J. S. Castrucci, K. B. Park, X. Bulliard, K. S. Kim, Y. W. Jin, S. Lee, T. P. Bender and S. Y. Park, *ACS Appl. Mater. Interfaces,* 2013, *5*, 13089–13095.

[17] H. O. Toshikatsu Sakai, H. Seo and T. Takagi, *MRS Adv.,* 2015, *1*, 459–464.

[18] S. J. Lim, D. S. Leem, K. B. Park, K. S. Kim, S. Sul, K. Na, G. H. Lee, C. J. Heo, K. H. Lee, X. Bulliard, R. I. Satoh, T. Yagi, T. Ro, D. Im, J. Jung, M. Lee, T. Y. Lee, M.

G. Han, Y. W. Jin and S. Lee, *Sci. Rep.,* 2015, **5**, 7708.

19 W. Li, D. Li, G. Dong, L. Duan, J. Sun, D. Zhang and L. Wang, *Laser Photonics Rev.,* 2016, **10**, 473–480.

20 W. Li, S. Li, L. Duan, H. Chen, L. Wang, G. Dong and Z. Xu, *Org. Electron.,* 2016, **37**, 346–351.

21 M. G. Han, K. B. Park, X. Bulliard, G. H. Lee, S. Yun, D. S. Leem, C. J. Heo, T. Yagi, R. Sakurai, T. Ro, S. J. Lim, S. Sul, K. Na, J. Ahn, Y. W. Jin and S. Lee, *ACS Appl. Mater. Interfaces,* 2016, **8**, 26143–26151.

22 W. Li, H. Guo, Z. Wang and G. Dong, *J. Phys. Chem. C,* 2017, **121**, 15333–15338.

23 C. W. Joo, J. Kim, J. Moon, K. M. Lee, J. E. Pi, S. Y. Kang, S. D. Ahn, Y. S. Park and D. S. Chung, *Org. Electron.,* 2019, **70**, 101–106.

24 G. H. Lee, X. Bulliard, S. Yun, D.-S. Leem, K.-B. Park, K.-H. Lee, C.-J. Heo, I.-S. Jung, J.-H. Kim, Y. S. Choi, S.-J. Lim and Y. W. Jin, *Opt. Express,* 2019, **27**, 25410–25419.

25 D. Shen, Z. Guan, M. Li, S.-W. Tsang, W. Zhang, M.-F. Lo and C.-S. Lee, *J. Mater. Chem. C,* 2021, **9**, 3814.

26 Y. Lin, Y. Firdaus, F. H. Isikgor, M. I. Nugraha, E. Yengel, G. T. Harrison, R. Hallani, A. El-Labban, H. Faber, C. Ma, X. Zheng, A. Subbiah, C. T. Howells, O. M. Bakr, I. McCulloch, S. De Wolf, L. Tsetseris, T. D. Anthopoulos, *ACS Energy Lett.,* 2020, **5**, 9, 2935–2944.

27 H. Kocer, S. Butun, Z. Li, and K. Aydin, *Sci. Rep.,* 2015**, 5**, 8157.

28 X. Wang, J. Wang, Z. D. Hu, T. Sang, and Y. Feng, *Appl. Phys. Express,* 2018, **11**, 6, 062601.

29 J. Ma, J. Wang, Z. D. Hu, Z. Zhang, L. Pan, A. Di Falco, *AIP Advances,* 2019, **9**, 115007.